Inorganic Chemistry

ARTICLE

pubs.acs.org/IC

High-Temperature Behavior and Polymorphism in Novel Members of the Perovskite Family Pb_2LnSbO_6 (Ln = Ho, Er, Yb, Lu)

Sebastián A. Larrégola,[†] José A. Alonso,*[,‡] Denis Sheptyakov,[§] Miguel Algueró,[‡] Angel Muñoz,[∥] Vladimir Pomjakushin,[§] and José C. Pedregosa[†]

[†]Área de Química General e Inorgánica "Dr. Gabino F. Puelles", Departamento de Química, Facultad de Química, Bioquímica, y Farmacia, Universidad Nacional de San Luis, Chacabuco y Pedernera, 5700 San Luis, Argentina

[‡]Instituto de Ciencia de Materiales de Madrid, C.S.I.C., Cantoblanco, 28049 Madrid, Spain

[§]Laboratory for Neutron Scattering, Paul Scherrer Institut, CH-5232 Villigen PSI, Switzerland

[∥]Departamento de Física Aplicada, EPS, Universidad Carlos III, Avda. Universidad 30, E-28911, Leganés-Madrid, Spain

Supporting Information

ABSTRACT: The synthesis, crystal structure, and dielectric properties of four novel members of the family of double perovskites Pb_2LnSbO_6 are described. The room-temperature crystal structures were refined from neutron powder diffraction (NPD) data in the monoclinic $C2/c$ (No. 15) space group. They contain a completely ordered array of alternating LnO_6 and SbO_6 octahedra sharing corners, tilted in antiphase along the three pseudocubic axes, with a $a^-b^-b^-$ tilting scheme, which is very unusual in the crystallochemistry of perovskites. The lead atoms occupy highly asymmetric voids with 8-fold coordination due to the stereoactivity of the Pb^{2+} electron lone-pair. Several trends are observed for the entire family of compounds upon heating. The Ln = Lu, Yb, and Er oxides display three successive phase transitions in a narrow temperature range, as shown by differential scanning calorimetry (DSC) data, while the Ln = Ho shows only two transitions. Different crystal structure evolutions have been found from temperature-dependent NPD and DSC, following the space-group sequence $C2/c \rightarrow P2_1/n \rightarrow R\bar{3} \rightarrow Fm\bar{3}m$ for Ln = Lu and Yb, the sequence $C2/c \rightarrow$ unknown $\rightarrow P2_1/n \rightarrow Fm\bar{3}m$ for Ln = Er, and $C2/c \rightarrow P2_1/n \rightarrow Fm\bar{3}m$ for Ln = Ho. The Ln/Sb long-range ordering is preserved across the consecutive phase transitions. Dielectric permittivity measurements indicate the presence of a paraelectric/antiferroelectric transition (associated with the last structural transition), as suggested by the negative Curie temperature from the Curie–Weiss fit of the reciprocal permittivity.

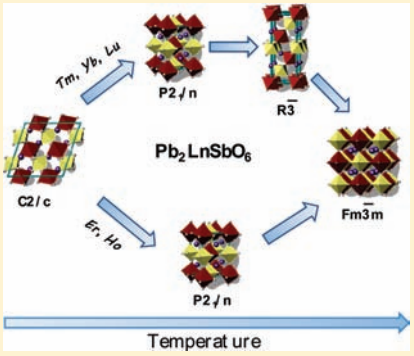

1. INTRODUCTION

Double perovskites $A_2B'B''O_6$ have been extensively studied due to their varied magnetic and electric properties. Their crystal structures present a tridimensional framework of corner-sharing $B'O_6$ and $B''O_6$ octahedra, where the A cations occupy the voids between every eight octahedra, in an ideal AO_{12} coordination. Whereas the simple ABO_3 perovskite is cubic, a large number of examples correspond to distorted perovskites with a lower symmetry. The causes of such distortion are related with three different phenomena:

(a) The octahedral tilting is the most common mechanism of distortion, due to the presence of too-small A atoms that drive the rotation of the $B'O_6$ and $B''O_6$ octahedra around one, two, or three crystalline axes in order to optimize the A–O bond lengths.

(b) Cation displacements from the center of their polyhedra are present. These asymmetric coordination environments are due to the presence of two particular types of cations: d^0 ions such as Ti^{4+}, Nb^{5+}, W^{6+}, etc., or p-block elements containing electron lone-pair, such as Pb^{2+}, Bi^{3+}, Sn^{2+}, Te^{4+}. In both cases, the main cause of such distortion is attributable to a second-order Jahn–Teller distortion (SOJT) due to electronic effects.[1−3] This kind of asymmetry induces technologically interesting properties, such as ferroelectricity, piezoelectricity, or nonlinear optics.

(c) The distortion of the octahedra is driven by electronic instabilities of the B-site cation, as occurs in the well-known Ba_2CuTeO_6[4] perovskite, where the presence of a first order Jahn–Teller distortion (i.e., Cu^{2+}, $3d^9$) induces the distortion of the CuO_6 octahedra, generating an elongation of the c-axis.

Many ABO_3 and $A_2B'B''O_6$ perovskites containing p-elements with an electron lone-pair at the A positions, exhibiting an irregular oxygen-coordination environment, require the use of high-pressure conditions to be stabilized. Actually, the well-known ferroelectric $PbTiO_3$ is the only Pb-3d transition metal perovskite that can be prepared at ambient pressures, while some other members such as $PbMnO_3$, $PbCrO_3$, or $PbVO_3$ have only

Received: January 19, 2011
Published: May 27, 2011

been recently stabilized under elevated pressures.[5] Concerning the double perovskites, two nice examples are Bi_2NiMnO_6[6] and Bi_2CoMnO_6,[7] prepared under pressure, where the presence of a lone pair induces cationic shifts that favor ferroelectricity: these materials are magneto-ferroelectrics, useful for multiple-memory devices (storage of information with both electrical and magnetic polarization) or electrically writable, magnetically readable magnetoelectric random-access memory devices. In some cases, the preparation of double perovskites containing p-block ions such as Pb^{2+} or Bi^{3+} is difficult due the possibility of producing the particularly stable pyrochlore phases. For instance, the hypothetical double perovskites Pb_2FeSbO_6 or Pb_2YNbO_6 have not been prepared yet because the synthesis invariably leads to the formation of $Pb_2Fe_{0.5}Sb_{1.5}O_{6.5}$[8] or Pb_2YNbO_7[9] competitive pyrochlore-like oxides.

By carefully choosing the nature of the B elements and the preparation conditions, we have been able to synthesize at ambient-pressure conditions and to describe some novel lead-containing double perovskite oxides. Pb_2ScSbO_6[10] is a cubic double perovskite that contains a completely ordered array of alternating ScO_6 and SbO_6 octahedra sharing corners and for which the PbO_{12} polyhedra display an off-center displacement of the lead atoms along the [111] direction. Also, two samples with stoichiometry $Pb_2Sc(Ti_{0.5}Te_{0.5})O_6$ and $Pb_3Sc_2TeO_9$ have been synthesized by solid-state techniques in air,[11] and similar structural features were observed in them for the PbO_{12} polyhedra. However, the effect of the antisite disorder over the B positions was found to be crucial for the relaxor-type dielectric response, showing a freezing temperature that depends on the antisite disordering degree.[11]

In our recent paper,[12] we have reported on the crystal structure, phase transitions, and dielectric properties of the first example of a novel series of double perovskites of composition Pb_2LnSbO_6 for Ln = Tm. At room temperature Pb_2TmSbO_6 exhibits a rare and highly distorted crystal structure described in the space group $C2/c$ (No. 15), presenting two different kinds of distortions: a tilting distortion, belonging to the $a^-b^-b^-$ tilting system as defined by Woodward,[13] and, additionally, the existence of an intraoctahedral distortion defined by a displacement of the Tm atom from the center of its octahedron along a $C2$ axis, which is first due to the asymmetric interaction with lead atoms; these atoms show an important displacement of 0.506 Å. Moreover, three successive phase transitions have been observed for this compound, which follows a novel polymorphic high-temperature sequence: $C2/c \rightarrow P2_1/n$ (i) $\rightarrow R\bar{3} \rightarrow Fm\bar{3}m$ [where $P2_1/n$ (i) means an incommensurate phase, which in a first approximation was described in the averaged structure with a $P2_1/n$ unit cell].

In the present work, we describe the synthesis and characterization of four new compounds belonging to the Pb_2LnSbO_6 family, with Ln = Lu, Yb, Er, and Ho, hereafter named PLSO, PYSO, PESO, and PHSO, respectively. They present the exotic $C2/c$ crystal structure at room temperature (rt) and several successive phase transitions as a function of temperature, across a number of polymorphs of increasing symmetry, which have been investigated by neutron and X-ray diffraction, and differential scanning calorimetry, complemented with dielectric permittivity measurements.

2. EXPERIMENTAL SECTION

Pb_2LnSbO_6 (Ln = Lu, Yb, Er, and Ho) were obtained by standard solid-state techniques; PbO, Ln_2O_3, Sb_2O_3 were used as starting materials. They were weighed out in the appropriate metal ratios and well-mixed in an agate mortar. The mixtures were calcined at 550 °C for 24 h in order to oxidize Sb^{3+} to Sb^{5+}. Subsequently, the products were heated at 800 and 900 °C for 12 h until single Pb_2LnSbO_6 phases were obtained. All the thermal treatments were carried out in sintered alumina crucibles and in air atmosphere. After all the calcination steps the samples were cooled down by switching off the furnace.

The initial structural identification and characterization of the samples were carried out by laboratory XRPD (Cu Kα, λ = 1.5406 Å) in a Bruker D8 Advance powder diffractometer with the Bragg−Brentano geometry. In addition, NPD data were collected on the HRPT high-resolution diffractometer (λ = 1.494 Å) at PSI. About 4 g of samples were placed in vanadium cans, and the counting time was typically 3 h per pattern. Room-temperature patterns were collected for all the samples, Ln = Ho, Er, Yb, and Lu. Additionally, temperature-dependent neutron diffraction studies have been carried out for the selected Ho, Er, and Yb samples in the temperature range rt < T < 550 K.

The refinement of the crystal structures was performed by the Rietveld method using the Fullprof suite.[14] The profile of the peaks was fitted by the Thompson−Cox−Hastings pseudo-Voigt function corrected for axial divergence asymmetry. The following parameters were refined in the final run of the fits: scale factor, background coefficients, zero-point error, pseudo-Voigt correction for asymmetry parameters, positional coordinates, isotropic displacement parameters, occupancy factors for lead and oxygen atoms, and antisite disordering between Ln and Sb atoms. The neutron coherent scattering lengths for Pb, Sb, and O are 9.405, 5.57, and 5.803 fm; for the lanthanide ions they are 7.21, 12.43, 7.79, and 8.01 fm for Lu, Yb, Er, and Ho, respectively.

The differential scanning calorimetry (DSC) study was performed in a Mettler TA3000 system equipped with a DSC30 unit. The measurements have been carried out during the heating and cooling runs from rt to 523 K with a rate of 10 K min^{-1} for powder samples encapsulated in standard Al crucibles. Additionally, experiments at three different heating/cooling rates (3, 5, 7 K min^{-1}) have been performed to study the order of the phase transitions of the Yb and Lu samples.

For the electrical measurements the samples have been cold-pressed at 2 GPa and then sintered at moderates temperatures (1073 K), in order to avoid the partial volatilization of PbO. Ag electrodes were painted on the major faces of thin ceramic disks and sintered at 873 K. The dependence of the dielectric permittivity on temperature was measured between 295 and 700 K with a HP4284A precision LCR meter. Measurements were dynamically carried out during a heating/cooling cycle at ±2 K min^{-1} rate at nine frequencies between 100 Hz and 1 MHz. Room-temperature, high electric field electrical properties were also studied. Voltage sine waves were applied (0.1 Hz frequency and amplitude up to 10 kV) by the combination of a synthesizer/function generator (HP 3325B) and a high-voltage amplifier (TREK model 10/40), and the charge was measured with a home-built charge to voltage converter and software for loop acquisition and analysis.

3. RESULTS

All the samples have been obtained in polycrystalline form with colors ranging from light yellowish for the Lu and Yb samples to light-orange for the Er and Ho materials. The four compounds display the same crystal structures at rt as Pb_2TmSbO_6, showing comparable XRPD patterns with slight differences in the unit-cell parameters. The patterns have been indexed in the monoclinic system, $C2/c$ (No. 15) space group, with the unit-cell parameters related to the aristotype ($a_0 \approx 4$ Å) as $a \approx c \approx \sqrt{6}a_0$ and $b \approx \sqrt{2}a_0$, which additionally can be derived from the program SPUDS for simple perovskites only.[15] The indexation of the Yb pattern is shown in Figure 1a; a comparison

dx.doi.org/10.1021/ic200127a |Inorg. Chem. 2011, 50, 5545–5557

between the XRPD patterns obtained for all the samples is displayed in Figure 1b.

3.1. Differential Scanning Calorimetry (DSC). The DSC curves obtained for the four compounds are presented in Figure 2. For all the samples no weight change has been observed after a heating/cooling cycle. Additionally, there are two distinct types of behaviors: The first one corresponds to PLSO and PYSO samples, which present three successive phase transitions following the same pattern as that previously reported for the Tm sample,[12] the first two processes being of first order and the last one of second order; in these two compounds the enthalpy ratio of the DSC peaks are $\Delta H_2/\Delta H_1 \approx 1.5$ and $\Delta H_2/\Delta H_3 \approx 10$ for both Ln = Lu and Yb. In order to determine the order of the phase transitions, DSC experiments at different heating rates have been performed for Yb and Lu samples (see Supporting Information Figure S.1). As previously observed for Pb_2TmSbO_6,[12] the first two transitions of Yb and Lu compounds present a first-order character, while the third phase transformation is second-order, since no thermal hysteresis is observed. On the other hand, PESO and PHSO present only two intense DSC peaks with an intensity ratio of approximately $\Delta H_2/\Delta H_1 \approx 5$, in contrast to the Ln = Tm, Yb, and Lu perovskites. Additionally, the erbium sample displays a tiny reversible peak at about 433 K, subtly differing from the holmium compound. The calculated enthalpies and entropies associated with each process are detailed in Table 1. Additionally, this table shows the enthalpy ratios between the different thermal events for each sample, which allows establishing a classification of the two kinds of thermal behaviors.

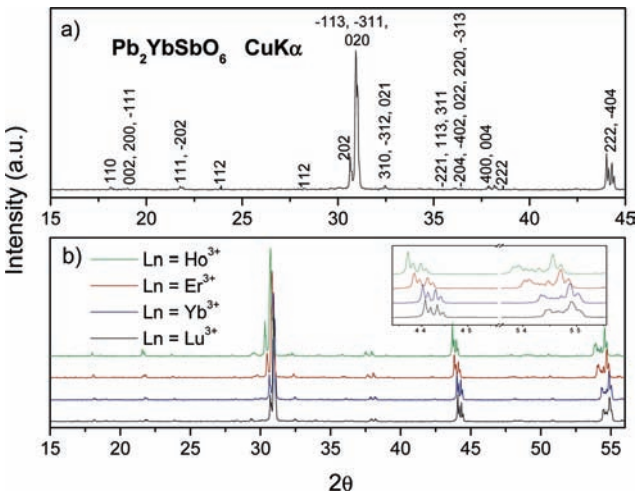

Figure 1. (a) X-ray powder diffraction (XRPD) pattern of Pb_2YbSbO_6, indexed in the monoclinic system, space group $C2/c$ (No. 15). (b) XRPD patterns obtained for the four compounds. Inset: expanded region between 22-55°.

Table 1. Transition Temperatures (on heating), Enthalpies and Entropies Obtained from the DSC Curves

parameter[a]	PLSO	PYSO	PTSO[12]	PESO	PHSO
T_1 (K)	337	355.5	387	409	425
T_2 (K)	424	433	446	456	470
T_3 (K)	461	465	462	436	
ΔH_1 (J/mol)	696.4	756.5	813	788	763
ΔH_2 (J/mol)	981.1	1256	1425	2150	3108
ΔH_3 (J/mol)	145.3	130.4	144.4	159	
ΔS_1 (J/K mol)	2.1	2.1	2.1	1.9	1.8
ΔS_2 (J/K mol)	2.3	2.9	3.2	4.7	6.6
ΔS_3 (J/K mol)	0.3	0.3	0.3	0.4	
$\Delta H_2/\Delta H_1$	1.4	1.7	1.7	2.8	4.2

[a] ΔH (l/g) = $\int_{T_i}^{T_f}(dH/dt)$ (W/g) dT (°C)/(dT/dt) (°C/s); ΔS (l/g °C) = ($\Delta H/T$),P = cte.

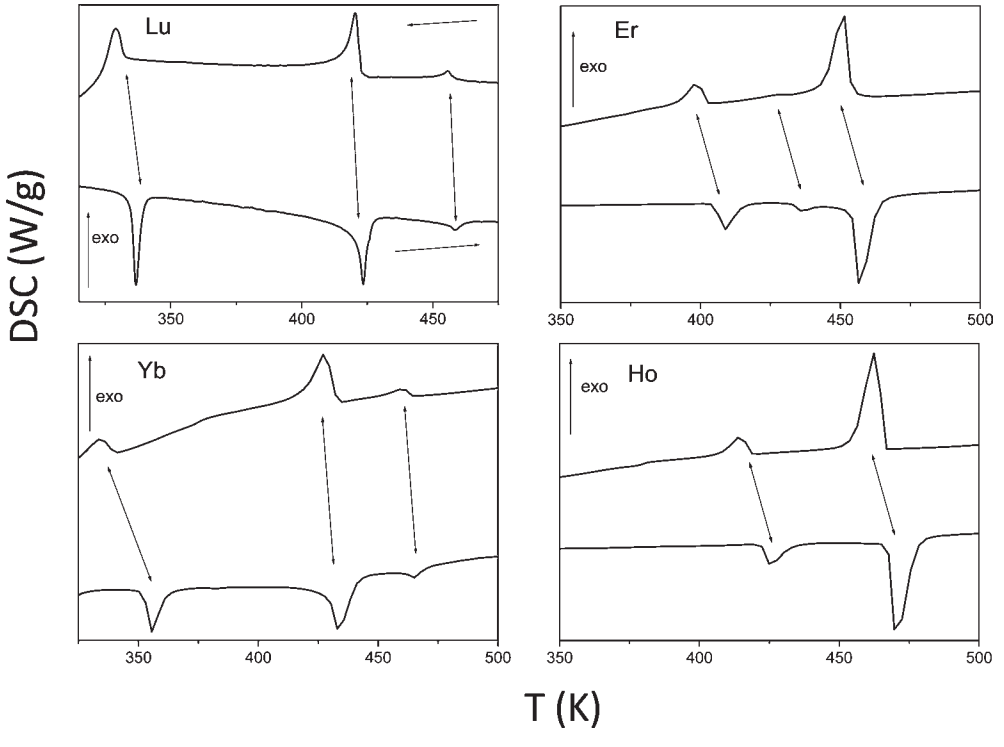

Figure 2. DSC plots showed by the samples. Endothermic peaks correspond to the heating process while exothermic peaks to the cooling run.

dx.doi.org/10.1021/ic200127a |Inorg. Chem. 2011, 50, 5545–5557

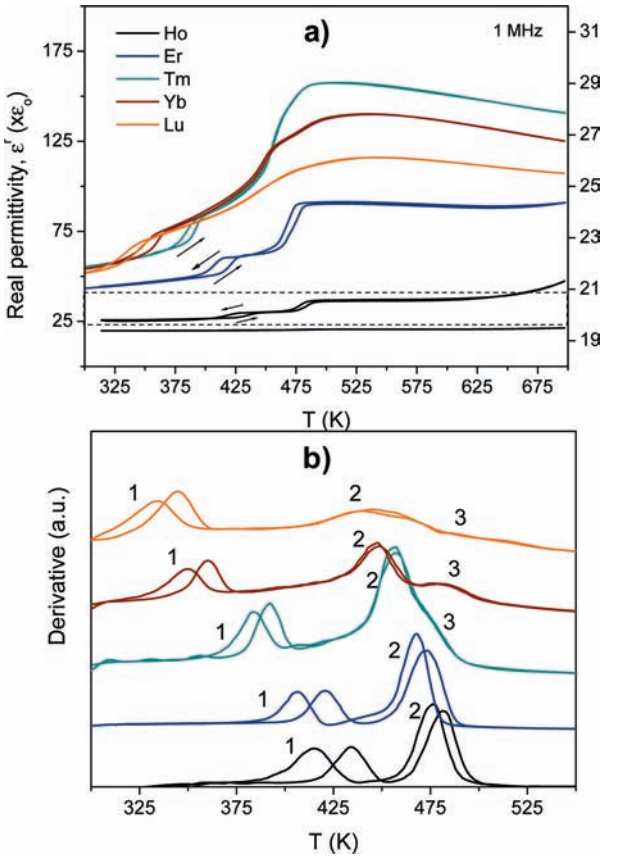

Figure 3. (a) Temperature dependence of the real permittivity of the Pb_2LnSbO_6 samples at 1 MHz. The arrows indicate the temperature progression. The scale on the right *y*-axis is for Ho curve between the dashed lines. (b) Derivative curves of the real permittivity data, where 1, 2, and 3 indicate the different phase transitions, as mentioned in the text.

3.2. Dielectric Permittivity Measurements. The real dielectric permittivity values for the series of double perovskites Pb_2LnSbO_6 with Ln = Ho, Er, Yb, and Lu, measured during a heating/cooling cycle between rt and 700 K, are shown in Figure 3a at 1 MHz. For the sake of comparison, the data for Tm are also included.[12] The polarizability of the perovskite with Ho is significantly lower than that of the four other compounds, and thus, its permittivity scale is expanded using the right *y*-axis (the curve between the dashed lines). The imaginary permittivity is given in Figure S.2 (Supporting Information). This parameter increases with temperature, but it does not exceed the value of 10 in any case, which correspond to a loss tangent <0.1. This clearly indicates that conductivity is not an issue in these data. Two clear, reversible dielectric anomalies are found for the double perovskites with Ho and Er, while three anomalies are observed in the case of the Tm, Yb, and Lu oxides that are associated with two and three successive phase transitions, respectively. From rt up to high temperature, Pb_2HoSbO_6 and Pb_2ErSbO_6 seem to undergo two clearly first-order phase transitions (referred to as 1 and 2 hereafter). Analogous dielectric anomalies are found for Pb_2TmSbO_6, Pb_2YbSbO_6, and Pb_2LuSbO_6, yet thermal hysteresis has mostly disappeared in the case of transition 2. Specific transition temperatures are better determined from the derivative plots, shown in Figure 3b.

In the case of the double perovskites with Tm, Yb, and Lu, there is a subsequent high-temperature transition (hereinafter referred to as 3) at a temperature which in this case increases with the lanthanide contraction. This is most probably a polar transition, as indicated by the good fit of the temperature dependence of the permittivity above 550 K to a Curie−Weiss behavior, shown in Figure S.3 (Supporting Information). This was carried out for the dielectric permittivity at the highest frequency of 1 MHz, in order to avoid conduction contributions present at lower frequencies, as illustrated in Figure S.4 (Supporting Information).

The polar nature of the room temperature phase was further studied with measurements of the ferroelectric (or antiferroelectric) loops. Loops typical of lossy dielectrics were obtained at fields up to 5 kV mm^{-1}, and higher fields could not be attained because electrical breakdown occurred. Results for Pb_2YbSbO_6 are shown in Figure S.5 (Supporting Information) as an example.

3.3. Structural Analysis. *3.3.1. Room Temperature Crystal Structures (P_α).* All the compounds possess the same crystal structure at room temperature as the one previously described for Pb_2TmSbO_6. In the corresponding structural model, Ln and Sb atoms are located at the 4e $(0,y,{}^1/_4)$ and 4c $({}^1/_4,{}^1/_4,0)$ Wyckoff sites, respectively, the oxygen atoms occupy three crystallographically nonequivalent positions located at 8f (x,y,z), and Pb atoms are also placed at the 8f (x,y,z) Wyckoff sites. Each LnO_6 octahedron is surrounded by six SbO_6 octahedra and vice versa; octahedral antiphase tiltings are observed in all the pseudocubic directions, corresponding to the $a^-b^-b^-$ Glazer notation.

Figure 4 shows Rietveld refinement plots for the samples, exhibiting an excellent agreement between observed and calculated profiles. A minor impurity of PbO_2 was detected and introduced as a second phase in the refinement, with a weight fraction of less than 2%. Table 2 lists the unit cell parameters, atomic positions, isotropic displacement factors, occupancy, and reliability factors. In addition, Table 3 contains the main bond lengths, some selected bond angles, and the tilting angles which were estimated as $\theta_C = (180 - \phi_c)/2$ (where ϕ_c is the average Sb−O−Ln angle defined by O2 and O3), $\theta_B = (180 - \phi_b)/2$ (where ϕ_b is the average Sb−O−Ln angle for O1 and O3), and $\theta_A = (180 - \phi_a)/2$ (where ϕ_a is the average Sb−O−Ln angle for O1 and O2), where the subindices A, B, and C represent the pseudocubic axis along which the tilt occurs.

3.3.2. High-Temperature Polymorphic Phases. Taking into account that there are two different types of structural thermal evolutions in the family, we describe those corresponding to two representative members.

a. Pb_2YbSbO_6 (PYSO). Polymorph β. First, it must be pointed out that from the comparison of the DSC measurements and the calculated thermodynamic variables associated with the crystal structure thermal evolution of this compound, it can be assumed that the Yb and Lu compounds present the same thermal behavior as Pb_2TmSbO_6, which follows the sequence $C2/c$ $(P_\alpha) \rightarrow P2_1/n$ (i) $(P_\beta) \rightarrow R\bar{3}$ $(P_\gamma) \rightarrow Fm\bar{3}m$ (P_δ).[12] The crystal structure of P_β for Ln = Yb has been refined from the NPD data at 393 K in the monoclinic system (SG $P2_1/n$, No. 14) with $Z = 2$. The unit-cell parameters obtained from the refinement for Ln = Yb were $a = 8.2433(1)$ Å, $b = 5.8304(1)$ Å, $c = 5.8836(1)$ Å and $\beta = 90.171(1)°$. They are related to the a_0 lattice constant of the aristotype as $b \approx c \approx \sqrt{2}a_0$ and $a \approx 2a_0$. The overall fit between observed and calculated profiles was very good, as shown in Figure 5. As observed for the P_β polymorph of Pb_2TmSbO_6, the crystal structure for Ln = Yb presents a

dx.doi.org/10.1021/ic200127a |*Inorg. Chem.* 2011, 50, 5545–5557

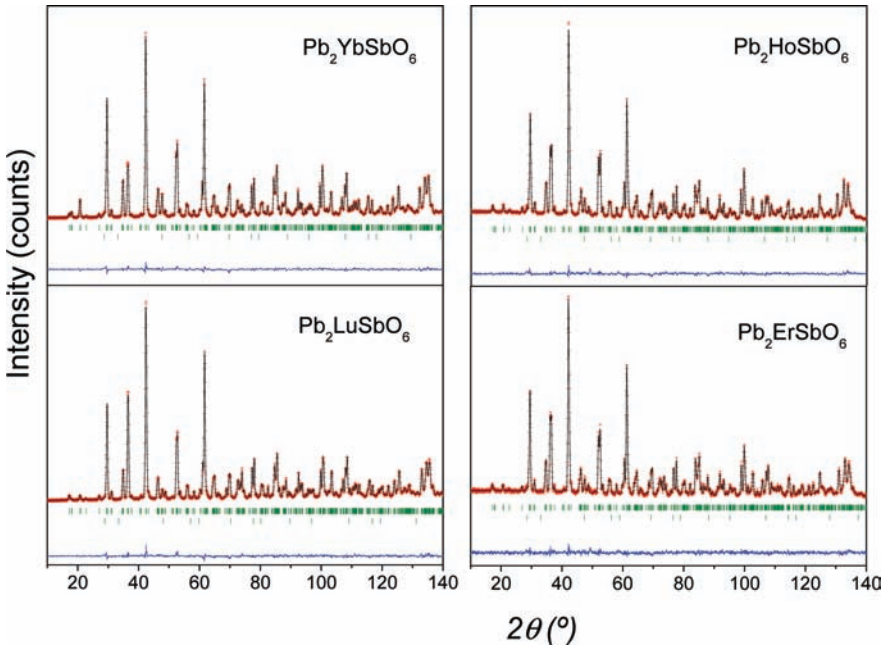

Figure 4. NPD Rietveld plots for the compounds Pb_2LnSbO_6 (Ln = Lu, Yb, Er and Ho) in the $C2/c$ space group at rt: observed (circles), calculated (solid line), and difference (bottom). The second rows of ticks correspond to the PbO_2 impurity phase with a weight fraction of less than 2%.

modulation that gives rise to a tiny peak in the temperature range between T_1 and T_2 (see inset of Figure 5 and Supporting Information Figure S.6). At the same time, in the X-ray diffraction patterns accumulated in the same phase, the number of the observable superstructure peaks is higher and their intensities are certainly stronger, which suggests that these superstructure peaks are originating probably from the (incommensurately modulated) shifts of the heaviest atoms in the structure (lead). Disregarding this tiny unsolved peak in the neutron powder data, the $P2_1/n$ model (commensurate subcell) describes satisfactorily the commensurate crystal substructure of the P_β polymorphs. Table 4 includes the unit cell parameters, atomic positions, isotropic thermal factors, occupancy, and reliability factors of the P_β structure. Table 5 lists the interatomic distances and some selected bond angles.

Polymorph γ. For the P_γ polymorph of the Yb compound, the refinement was carried out from the NPD data at 452 K, corresponding to the temperature region at the plateau between the T_2 and T_3 observed at the DSC curve (Figure 2). The structure can be defined in the $R\bar{3}$ space group (No. 148), corresponding to a slight rhombohedral distortion of the double perovskite. The unit cell parameters in the hexagonal setting are $a = b = 5.86081(5)$ Å, $c = 14.3166(2)$ Å and $\alpha = \beta = 90°$ and $\gamma = 120°$. In the structural model, Pb atoms occupy the special positions 2c (x,x,x), while the Yb and Sb atoms occupy the 1a (0,0,0) and 1b ($^1/_2$,$^1/_2$,$^1/_2$) Wyckoff sites, respectively, and a single type of oxygen atoms is located at 6f (x,y,z) positions. Figure 6a displays the Rietveld plot of P_γ, exhibiting a quite satisfactory fit between observed and calculated profiles. The inset of Figure 6a shows a schematic view of the crystal structure of this rhombohedral polymorph. Table 4 contains the unit cell parameters, atomic positions, isotropic displacement factors, occupancy, and reliability factors. Table 5 includes the interatomic distances and some selected bond angles.

Polymorph δ. The crystal structure sequence concludes in the cubic system, with a doubling of the unit cell parameters ($a = b = c = 2a_0$), as defined in the well-known $Fm\bar{3}m$ space group for double perovskites (elpasolite structure). In this model, Yb and Sb atoms were located at the 4a (0,0,0) and 4b ($^1/_2$,0,0) Wyckoff sites, respectively, O atoms are placed at the 24e sites $(x,0,0)$, and Pb atoms occupy the 32f (x,x,x) positions, presenting a subtle off-center displacement along the [111] direction, similar to that reported for Pb_2ScSbO_6.[10] The Rietveld plot of the NPD refinement is displayed at Figure 6b; Table 4 contains the determined unit cell parameters, atomic positions, isotropic displacement factors, occupancy, and reliability factors. Table 5 contains the main bond lengths and some selected bond angles.

b. Pb_2HoSbO_6 (PHSO). In this case, the most important difference is the absence in the thermal structural sequence of the rhombohedral polymorph (P_γ). This perovskite presents two instead three successive phase transitions, following the sequence $C2/c$ (P_α) → $P2_1/n$ (P_β) → $Fm\bar{3}m$ (P_δ). Figure 7 shows the complete thermal evolution of the NPD patterns as contour surfaces, and the transition temperatures are marked with lines.

c. Pb_2ErSbO_6 (PESO). This sample presents almost the same structural evolution as PHSO. The P_β and P_δ polymorphic phases are isostructural to those observed for the Yb sample; the refinements were successfully carried out with the above-described structural models. The Rietveld plots of the P_β and P_δ polymorphs for Ln = Ho, Er, showing satisfactory fits, are displayed in the Supporting Information as Figures S.7 and S.8. It is noteworthy that the modulated phase (P_β) shows a more intense incommensurate peak for Ln = Ho, Er, so a greater contribution of the modulation is expected. The more conspicuous difference existent between the Er and Ho samples is that the former presents a very weak additional DSC peak at $T_3 = 436$ K. This endothermic peak, observed only in the DSC curve of this sample, has a reversible character and a tiny intensity. No substantial changes were observed in the NPD patterns above and below the T_3 transition temperature. Additionally, in our separate synchrotron X-ray powder diffraction investigation of

dx.doi.org/10.1021/ic200127a |*Inorg. Chem.* 2011, 50, 5545–5557

Table 2. Unit Cell, Positional, and Displacement Parameters for the P_α in the Monoclinic $C2/c$ Space Group, from NPD at 295 K for PLSO, PYSO, PESO, and PHSO

parameters	PLSO	PYSO	PESO	PHSO
a (Å)	10.11241(2)	10.13133(1)	10.17585(3)	10.19955(2)
b (Å)	5.81492(1)	5.81894(1)	5.83356(1)	5.83886(1)
c (Å)	10.09729(1)	10.11603(1)	10.15705(2)	10.17735(1)
β (deg)	108.8743(1)	108.8143(1)	108.7182(1)	108.6628(1)
vol (Å^3)	561.84(1)	564.51(1)	571.05(1)	574.23(1)
R_p	7.14	5.82	11.2	7.42
R_{wp}	7.95	6.39	11.5	7.79
R_{exp}	6.22	4.08	10.08	5.36
R_{BRAGG}	3.06	2.71	3.71	3.51
χ^2	1.63	2.45	1.31	2.12
Pb				
x	0.1300(1)	0.1303(1)	0.1307(2)	0.1311(1)
y	0.7790(2)	0.7796(1)	0.7810(2)	0.7817(1)
z	0.1274(2)	0.1273(1)	0.1270(2)	0.1269(2)
B_{iso} (Å^2)	1.03(2)	0.95(1)	1.03(3)	1.02(2)
Ln				
x	0	0	0	0
y	0.2530(2)	0.2531(1)	0.2536(4)	0.2534(2)
z	1/4	1/4	1/4	1/4
B_{iso} (Å^2)	0.34(4)	0.31(2)	0.49(5)	0.26(3)
Sb				
x	1/4	1/4	1/4	1/4
y	1/4	1/4	1/4	1/4
z	0	0	0	0
B_{iso} (Å^2)	0.24(4)	0.17(3)	0.14(6)	0.32(4)
O1				
x	0.1037(2)	0.1034(2)	0.1031(3)	0.1032(2)
y	0.2138(4)	0.2124(3)	0.2088(4)	0.2066(3)
z	0.0899(2)	0.0894(2)	0.0879(3)	0.0867(2)
B_{iso} (Å^2)	0.91(2)	0.87(2)	0.80(4)	0.92(3)
O2				
x	0.1449(2)	0.1453(2)	0.1462(3)	0.1476(2)
y	0.0304(4)	0.0317(3)	0.0354(5)	0.0367(4)
z	0.8531(2)	0.8527(2)	0.8510(3)	0.8502(2)
B_{iso} (Å^2)	1.00(3)	1.02(3)	1.23(5)	1.22(3)
O3				
x	0.3475(2)	0.3465(2)	0.3445(3)	0.3438(2)
y	0.0139(4)	0.0139(3)	0.0165(5)	0.0159(4)
z	0.6184(2)	0.6176(2)	0.6155(3)	0.6142(2)
B_{iso} (Å^2)	0.86(3)	0.82(3)	1.00(4)	1.07(3)

Table 3. Main Interatomic Distances (Å) and Angles (deg) Obtained for the P_α Polymorphs at 295 K

	Lu	Yb	Er	Ho
		Pb Polyhedron		
Pb−O1	3.309(3)[a]	3.324(2)[a]	3.363(3)[a]	3.384(2)[a]
Pb−O1	2.557(3)	2.549(2)	2.528(3)	2.515(2)
Pb−O1	2.656(2)	2.659(2)	2.664(3)	2.669(2)
Pb−O1	3.250(2)[a]	3.264(2)[a]	3.296(3)[a]	3.312(2)[a]
Pb−O2	3.179(3)[a]	3.188(3)[a]	3.220(4)[a]	3.237(3)[a]
Pb−O2	3.059(3)	3.067(3)	3.089(4)	3.112(3)
Pb−O2	2.494(3)	2.490(3)	2.473(4)	2.464(3)
Pb−O2	2.857(3)	2.863(2)	2.878(4)	2.875(3)
Pb−O3	2.535(3)	2.528(2)	2.510(4)	2.509(3)
Pb−O3	2.992(3)	2.993(3)	2.985(4)	2.983(3)
Pb−O3	3.027(3)	3.040(2)	3.081(4)	3.098(3)
Pb−O3	3.302(3)[a]	3.318(2)[a]	3.361(4)[a]	3.374(3)
⟨Pb−O⟩	2.772	2.773	2.776	2.778
		LnO_6		
Ln−O1 (×2)	2.204(2)	2.212(2)	2.233(3)	2.250(2)
Ln−O2 (×2)	2.227(2)	2.238(2)	2.265(4)	2.279(2)
Ln−O3 (×2)	2.158(2)	2.169(2)	2.187(3)	2.203(2)
⟨Ln−O⟩	2.196	2.206	2.228	2.244
O1−Ln−O1	168.1(2)	167.7(2)	166.6(3)	166.0(2)
O2−Ln−O2	84.5(1)	84.4(1)	83.8(2)	83.9(1)
O3−Ln−O3	102.2(1)	102.6(1)	104.3(2)	104.6(1)
O2−Ln−O3	169.7(2)	169.4(2)	168.0(3)	167.6(2)
		SbO_6		
Sb−O1 (×2)	1.982(2)	1.984(2)	1.986(3)	1.982(2)
Sb−O2 (×2)	1.985(2)	1.985(2)	1.987(3)	1.987(2)
Sb−O3 (×2)	1.998(2)	1.995(2)	1.998(3)	1.992(2)
⟨Sb−O⟩	1.988	1.988	1.990	1.987
O1−Sb−O1	180.0(2)	180.0(2)	180.0(3)	180.0(2)
O2−Sb−O2	180.0(2)	180.0(2)	180.0(3)	180.0(2)
O3−Sb−O3	180.0(2)	180.0(2)	180.0(3)	180.0(2)
O2−Sb−O3	89.7(1)	89.7(2)	89.7(2)	89.7(1)
		Angles around O		
Ln−O1−Sb	158.1(1)	157.6(1)	156.4(1)	155.7(1)
Ln−O2−Sb	159.6(1)	159.2(1)	157.7(1)	156.8(1)
Ln−O3−Sb	165.2(1)	164.8(1)	163.6(1)	163.5(1)
θ_A	−10.6	−10.8	−11.5	−11.9
θ_B	−9.2	−9.4	−10	−10.2
θ_C	−8.8	−9	−9.7	−9.9

[a] Disregarded distance.

the title compounds,[16] we have noticed that the nature of the transition associated with T_3 may probably be associated with the temperature-independent (below T_3) to temperature-dependent (above T_3) modulation of the crystal structure, while both below and above T_3 the average monoclinic $P2_1/n$ commensurate subcell model fits satisfactorily the positions and intensities of the major peaks.

It is worth mentioning that during the structural refinements of all the polymorphs the possibility of antisite disorder of the two B-type cations was investigated. Without exception all the refinements indicated a complete ordering of Ln and Sb cations over the two B sites. This is expected from the large size difference between Ln^{3+} and Sb^{5+} cations. On the other hand, the refinement of the oxygen site fractional occupancies gave a value of unity (within the standard deviations) for all the cases; hence, the occupancies were subsequently fixed to this value.

4. DISCUSSION

4.1. Room Temperature Crystal Structures. The four members reported in this paper present the same room temperature crystal structure, which is an uncommon monoclinic structure (space group $C2/c$) only adopted by a few simple perovskites, i.e. $BiMnO_3$ and $BiScO_3$,[17,18] both synthesized under high-pressure

dx.doi.org/10.1021/ic200127a |Inorg. Chem. 2011, 50, 5545–5557

conditions. We have reported in a previous paper the first example of a double perovskite that adopts this crystal structure, of composition Pb_2TmSbO_6. The unit cell parameters of the four compounds vary monotonically with the lanthanide ionic radii, as shown in Figure 8. This structural distortion is characterized by various kinds of structural peculiarities, which include the octahedral tilting, the LnO_6 intraoctahedral distortion, and the lead atom displacement in the PbO_{12} void. As has been mentioned in a previous section, this structure adopts the $a^-b^-b^-$ tilt system in Glazer's notation. The calculated tilting angles for the four compounds have similar values to those reported for Pb_2TmSbO_6, which increase with the increment of the monoclinic distortion, driven by the increase of the lanthanide ionic radii (see Figure 9). The most relevant peculiarities of this structure are determined by this distortion and probably by the stereoactivity of the Pb lone electron pair.

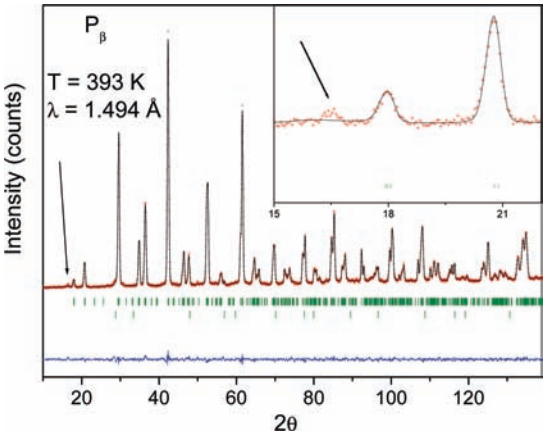

Figure 5. Observed (circles), calculated (solid line), and difference (bottom) profile after a Rietveld refinement of the NPD data for the P_β polymorph of Pb_2YbSbO_6 measured at 393 K. The inset shows the unsolved incommensurate peak.

The lead polyhedron presents an eight-coordinated environment (disregarding distances longer than 3.1 Å) with an important off-center lead displacement due to the asymmetry introduced by the highly stereochemically active $6s^2$ lone pair, as has been observed for Pb_2TmSbO_6. From the Pb−O distances presented in Table 3, a group of four shorter Pb−O distances is observed in the four cases, revealing the displacement direction, which occurs toward four adjacent oxygen atoms of the aristotype following the direction established by the vector $[1,{}^3/_5,{}^2/_5]$

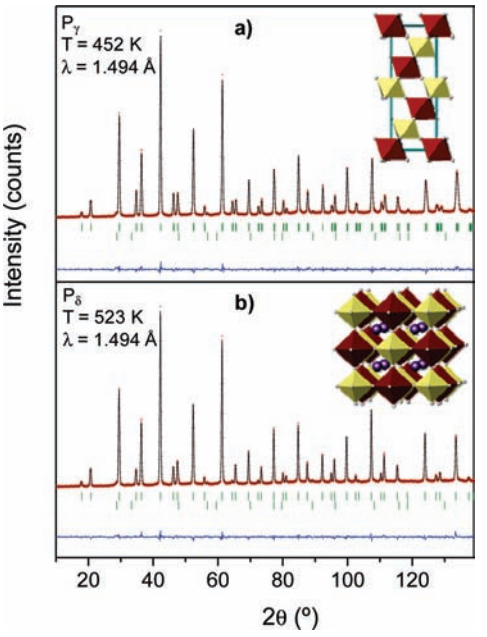

Figure 6. Observed (circles), calculated (solid line), and difference (bottom) profiles after a Rietveld refinement of the NPD data for (a) P_γ polymorph of Pb_2YbSbO_6 measured at 452 K and (b) P_δ polymorph measured at 523 K. Both insets show the schematic view of the rhombohedral $R\bar{3}$ and cubic $Fm\bar{3}m$ crystal structures of the Yb sample.

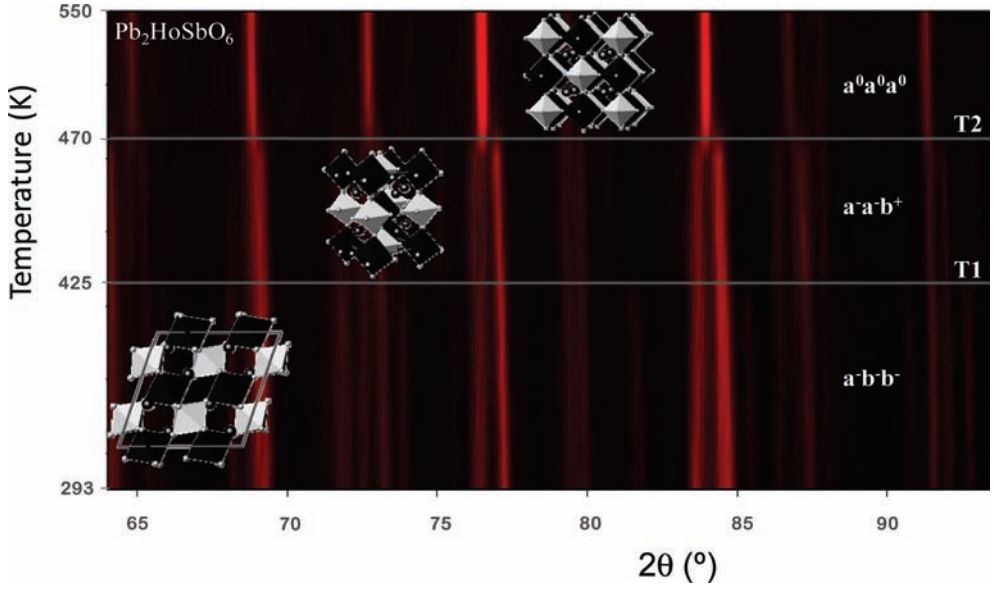

Figure 7. Contour graph of the thermal evolution of the neutron diffraction patterns of Pb_2HoSbO_6 from rt to 523 K. The horizontal solid lines represent the phase transition temperatures and the crystal structures correspond to the three observed polymorphs for this sample.

dx.doi.org/10.1021/ic200127a |*Inorg. Chem.* 2011, 50, 5545–5557

Table 4. Unit Cell, Positional, and Thermal Parameters for Pb_2YbSbO_6 in the Monoclinic $P2_1/n$, Rhombohedral $R\bar{3}$, and Cubic $Fm\bar{3}m$ Space Groups, from NPD Data at 393, 452, and 523 K, Respectively, and for Pb_2HoSbO_6 and Pb_2ErSbO_6 in the Monoclinic $P2_1/n$ and Cubic $Fm\bar{3}m$ Space Groups at 420−550 and 450−520 K, Respectively

	Yb			Ho		Er	
	P_β	P_γ	P_δ	P_β	P_δ	P_β	P_δ
a (Å)	8.2433(1)	5.86081(5)	8.29307(5)	8.30596(6)	8.3581(1)	8.28532(6)	8.32447(5)
b (Å)	5.8304(1)	$=a$	$=a$	5.86585(4)	$=a$	5.85623(4)	$=a$
c (Å)	5.8836(1)	14.3166(2)	$=a$	5.93199(3)	$=a$	5.90730(3)	$=a$
β (deg)	90.171(1)	–	90.00	90.2033(3)	90.00	90.1806(2)	90.00
vol (Å^3)	282.78(1)	425.88(1)	570.36(1)	289.01(1)	583.89(1)	286.62(2)	576.85(3)
R_p	8.48	11.2	12.3	16.6	19.5	21.7	22.4
R_{wp}	8.74	9.7	10.1	15.3	14.0	18.4	16.2
R_{exp}	6.55	7.6	7.73	11.9	12.6	14.1	14.3
R_{BRAGG}	2.21	2.25	1.97	4.93	2.33	5.94	1.85
χ^2	1.78	1.62	1.71	1.67	1.24	1.69	1.27
Pb							
x	0.2520(5)	0	0.2352(6)	0.253(1)	0.234(1)	0.253(1)	0.236(5)
y	0.5002(8)	0	$=x$	0.510(2)	$=x$	0.504(2)	$=x$
z	−0.0040(5)	0.2515(5)	$=x$	−0.002(1)	$=x$	−0.006(1)	$=x$
B_{iso} (Å^2)	2.4(2)	2.5(1)	2.0(2)	3.5(3)	3.9(2)	2.6(3)	2.5(2)
Ln							
x	0	0	0	0	0	0	0
y	0	0	0	0	0	0	0
z	0	0	0	0	0	0	0
B_{iso} (Å^2)	0.46(3)	0.72(4)	0.49(5)	0.7(3)	1.4(3)	0.5(3)	0.9(1)
Sb							
x	$^1/_2$	0	$^1/_2$	$^1/_2$	$^1/_2$	$^1/_2$	$^1/_2$
y	0	0	0	0	0	0	0
z	0	$^1/_2$	0	0	0	0	0
B_{iso}(Å^2)	0.13(7)	0.23(3)	0.14(6)	0.8(3)	0.8(3)	0.5(1)	0.14(8)
O1							
x	0.032(1)	−0.1437(5)	0.2633(2)	0.023(2)	0.2653(3)	0.028(2)	0.2651(3)
y	0.259(2)	−0.353(1)	0	0.264(3)	0	0.239(2)	0
z	0.733(2)	−0.0878(4)	0	0.736(3)	0	0.721(2)	0
B_{iso}(Å^2)	2.3(2)	2.7(2)	3.5(4)	2.8(3)	4.1(4)	1.8(3)	3.8(4)
O2							
x	0.7643(4)	–	–	0.766(1)	–	0.764(1)	–
y	0.495(2)	–	–	0.494(3)	–	0.482(2)	–
z	0.5534(5)	–	–	0.555(1)	–	0.552(1)	–
B_{iso} (Å^2)	2.1(3)	–	–	1.7(4)	–	1.7(2)	–
O3							
x	0.025(1)	–	–	0.031(1)	–	0.028(2)	–
y	0.736(2)	–	–	0.736(2)	–	0.734(3)	–
z	0.736(2)	–	–	0.723(2)	–	0.747(2)	–
B_{iso} (Å^2)	2.3(3)	–	–	2.9(2)	–	3.0(3)	–

from the geometrical center of the void. In these four shorter Pb−O bond lengths there is a subgroup that includes the three shortest distances around 2.5 Å and another bond length of approximately 2.65 Å (see Table 3). Figure 10 illustrates the environment of the lead atoms with its displacement direction marked with an arrow; in addition, an empty region is observed that is probably occupied by the $6s^2$ lone pair of lead atoms, as suggested in Figure 10. Taking into account the three shortest Pb−O bond lengths, the displacement pattern could be seen as a PbO_3E environment, where E represents the lone pair (see Figure 10b). These unexpectedly short Pb−O bond lengths are consistent with previously reported values for highly hybridized systems such as PbO[19] and simple perovskites, which present a strong hybridization between Pb 6s-states and oxygen p-states, such as $PbRuO_3$.[20,21]

There is a clear evolution of the magnitude of the lead displacement with the monoclinic distortion. In Figure 11 the lead displacement and the shortest ⟨Pb−O⟩ bond length are plotted versus the tolerance factor of the perovskite structure. Figure 11 shows that an increment of the distortion (i.e., a

dx.doi.org/10.1021/ic200127a |Inorg. Chem. 2011, 50, 5545–5557

Table 5. Main Interatomic Distances (Å) and Angles (deg) for Pb_2YbSbO_6 in the Monoclinic $P2_1/n$, Rhombohedral $R\bar{3}$, and Cubic $Fm\bar{3}m$ space groups, from NPD data at 393, 452, and 523 K, Respectively, and for Pb_2HoSbO_6 and Pb_2ErSbO_6 in the Monoclinic $P2_1/n$ and Cubic $Fm\bar{3}m$ Space Groups at 420−550 and 450−520 K, Respectively

	Yb			Ho		Er	
	P_β	P_γ	P_δ	P_β	P_δ	P_β	P_δ
			PbO_{12} Polyhedra				
Pb−O1	2.75(1)	(×3) 2.882(3)	(×6) 2.937(5)	2.85(2)	(×6) 2.96(1)	2.91(5)	(×6) 2.95(4)
Pb−O1	2.70(1)	(×3) 2.721(3)	(×3) 2.768(5)	2.77(2)	(×3) 2.77(1)	2.61(1)	(×3) 2.79(4)
Pb−O1	3.16(1)[a]	(×3) 2.985(3)	(×3) 3.114(5)	3.10(2)[a]	(×3) 3.16(1)	3.24(1)[a]	(×3) 3.12(1)
Pb−O1	3.10(1)[a]	(×3) 3.143(3)[a]	–	3.10(2)[a]	–	2.99(1)	–
Pb−O2	3.23(5)[a]	–	–	3.28(9)[a]	–	3.23(1)[a]	–
Pb−O2	2.66(1)	–	–	2.66(1)	–	2.68(1)	–
Pb−O2	2.90(2)	–	–	2.98(2)	–	2.87(1)	–
Pb−O2	2.97(2)	–	–	2.93(2)	–	3.03(1)	–
Pb−O3	2.78(1)	–	–	2.79(1)	–	2.72(2)	–
Pb−O3	2.76(1)	–	–	2.75(1)	–	2.80(2)	–
Pb−O3	3.10(1)[a]	–	–	3.22(1)[a]	–	3.12(2)[a]	–
Pb−O3	3.06(1)	–	–	3.05(1)		3.12(2)[a]	
⟨Pb−O⟩	2.93	2.93	2.94	2.956	2.94	2.94	2.952
$\langle Pb-O\rangle_{short}$	2.82	–	–	2.85	–	2.83	–
			LnO_6 Octahedra				
Ln−O_1	(×2) 2.19(1)	(×6) 2.168(3)	(×6) 2.184(2)	(×2) 2.21(2)	(×6) 2.217(3)	(×2) 2.17(1)	(×6) 2.207(2)
Ln−O_2	(×2) 2.19(3)	–	–	(×2) 2.23(1)	–	(×2) 2.21(1)	–
Ln−O_3	(×2) 2.21(1)	–	–	(×2) 2.26(1)	–	(×2) 2.17(2)	–
⟨Ln−O⟩	2.197	2.168	2.184	2.23	2.217	2.183	2.207
			Angles around Ln				
O1−Ln−O1	180.0(9)	180.0(3)	180.0	180.0(1)	180.0	180.0(9)	180.0
O1−Ln−O2	91.9(6)	–	–	90.3(9)	–	91.8(7)	–
O1−Ln−O2	88.1(5)	–	–	89.7(9)	–	88.2(6)	–
O1−Ln−O3	92.0(7)	–	–	92.6(6)	–	94.1(7)	–
			SbO_6 Octahedra				
Sb−O_1	(×2) 1.98(1)	(×6) 1.995(3)	(×6) 1.963(2)	(×2) 1.98(2)	(×6) 1.962(3)	(×2) 2.02(1)	(×6) 1.955(2)
Sb−O_2	(×2) 1.975(3)	–	–	(×2) 1.98(1)	–	(×2) 1.98(1)	–
Sb−O_3	(×2) 1.95(1)	–	–	(×2) 1.94(1)	–	(×2) 1.99(1)	–
⟨Sb−O⟩	1.968	1.995	1.963	1.966	1.962	1.996	1.955
			Angles around Sb				
O1−Sb−O1	180.0(5)	180.0(3)	180.0	180.0(2)	180.0(2)	180.0(1)	180.0
O1−Sb−O2	90.3(6)	–	–	87.9(1)	–	88.3(7)	–
O1−Sb−O2	89.7(7)	–	–	92.1(1)	–	91.7(7)	–
O1−Sb−O3	89.6(7)	–	–	89.7(1)	–	91.9(1)	–
O1−Sb−O3	90.4(8)	–	–	90.3(1)	–	88.1(8)	–
			Angles around O				
Ln−O_1−Sb	165.2(4)	167.9(1)	180.0(1)	165.4(5)	180.0(1)	164.5(4)	180.0
Ln−O_2−Sb	162.6(1)	–	–	162.1(3)	–	162.2(3)	–
Ln−O_3−Sb	168.8(4)	–	–	169.6(7)	–	166.9(6)	–
θ_A	−8	−6.1	0	−8.1	0	−8.3	0
θ_B	−6.5	−6.1	0	−6.3	0	−7.1	0
θ_C	7	−6.1	0	7.1	0	7.7	0

[a] Disregarded bond distance.

decrease of the tolerance factor) induces a greater lead shift and a shorter Pb−O bond length. This trend is opposite to what would be expected from the unit cell parameter variation, where the shorter Pb−O bond lengths should be the longest for Ho in the series, exhibiting the highest unit cell volume. The observed behavior can be understood as a product of the chemical pressure

dx.doi.org/10.1021/ic200127a |Inorg. Chem. 2011, 50, 5545–5557

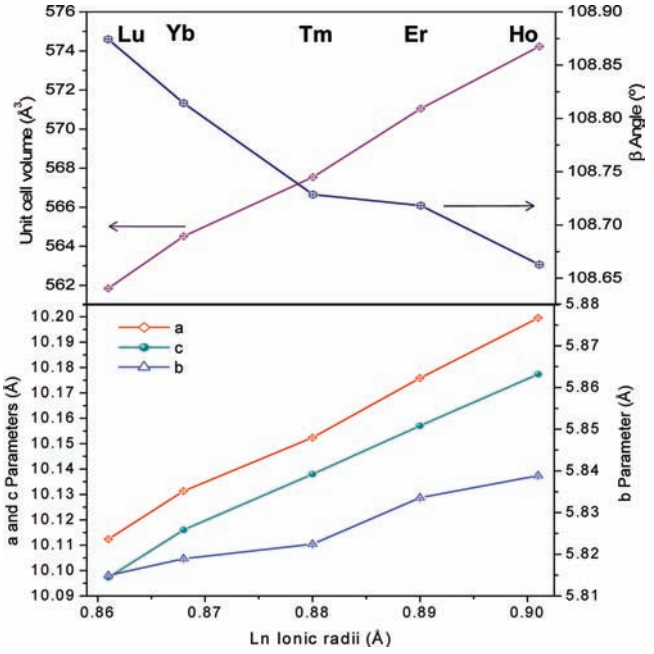

Figure 8. Evolution with the lanthanide ionic radii of the (a) unit cell volume and monoclinic β angle and (b) unit cell parameters. Both a and b graphs correspond to the room-temperature $C2/c$ polymorphs.

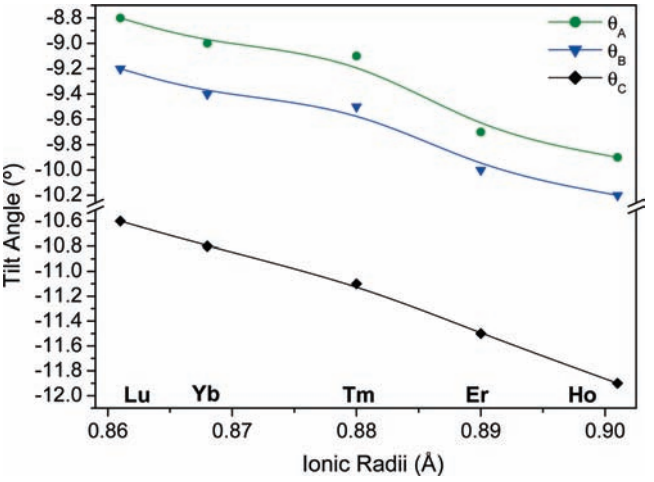

Figure 9. Evolution with the lanthanide ionic radii of the tilting angles θ_A, θ_B, and θ_C through the [100], [010], and [001] pseudocubic directions, respectively, in the room temperature $C2/c$ polymorphs of Pb_2LnSbO_6 (Ln = Ho, Er, Tm, Yb, and Lu).

supported by the lead lone pair in the empty region with the increment of the monoclinic distortion.

Another consequence of the strong distortion is the Ln-shifting observed in the LnO_6 octahedron. From the data listed in Table 3, the Ln−O distances can be classified into three groups of two long, two medium, and two short bond lengths, which are characteristic of a displacement along the local $C2$ [110] direction of the octahedron.[22] In the case of Pb_2TmSbO_6[12] we have observed that this displacement is driven by the asymmetric interaction that exists between oxygen and the shifted lead atoms through the path $Ln-O-(Pb)_n$, where some oxygen atoms are bonded to one or two lead atoms. Figure 12

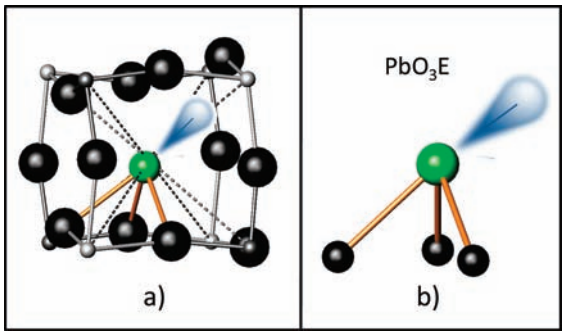

Figure 10. (a) Schematic view highlighting the displacement of a lead atom in the void between eight octahedra for the α polymorph. (b) The lead atoms environment PbO_3E generated by the three shorter Pb−O bond distances and the lone pair. The possible orientation of the $6s^2$ lone pair is indicated in both figures.

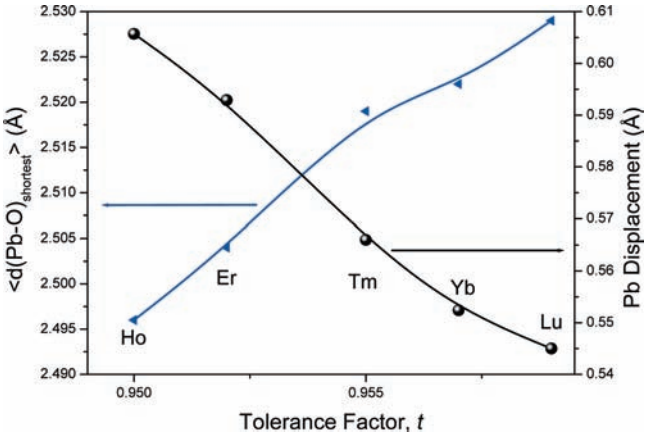

Figure 11. The observed relationship between the lead atom displacements inside the polyhedron and the shortest Pb−O bond length to the tolerance factor of the perovskite structure.

illustrates the dependence of the Ln-shifting on the value of the shortest ⟨Pb−O⟩ bond lengths for the five compounds of the family. This observed trend is an important evidence of the relationship between the lanthanide ionic size and the lead atom shifting, taking into account that in several cases the shifting of metals in octahedral coordination seems to appear due to the interaction with a lone-pair element or with the oxygen anions that are linked to the lone-pair element. Two different perspectives of the LnO_6 octahedron are included as insets in Figure 12. There are two different Pb−O interactions, bonded to two or one oxygen atoms in each octahedron, that could account for the deformation of the LnO_6 octahedron.

It is essential to remark that both octahedral sites are different in symmetry. The Sb atom is located at a center of symmetry. Therefore, the O−Sb−O bond angles with the opposite oxygen atoms are constrained to be 180° by the space group symmetry, while the Ln site has only a 2-fold rotational symmetry (inset of Figure 12).

In order to evaluate the octahedral distortion of the LnO_6 units, the Δd parameter has been calculated for all the samples using the equation defined in ref 22. Two different Δd values have been observed: for Lu, Yb, and Tm samples $\Delta d = 0.14$, while for the Ho and Er perovskites, Δd is 0.16. These values fall into

dx.doi.org/10.1021/ic200127a |Inorg. Chem. 2011, 50, 5545–5557

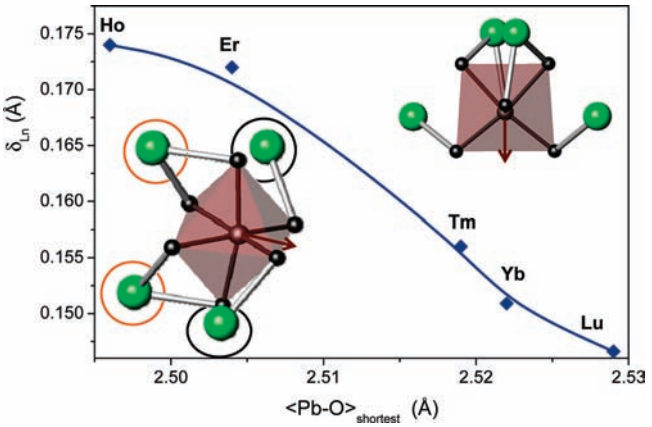

Figure 12. Experimental dependence of the lanthanide atom displacement (δ_{Ln}) in the octahedron on the shortest Pb−O bond length value. The insets show two different perspectives of a LnO_6 octahedron, and the lanthanide shifting directions are marked with arrows.

the first category defined by Halasyamani,[22] with a magnitude located in the range of $0.05 < \Delta d < 0.4$; following the criteria proposed by the author, this figure corresponds to a *weak magnitude* of octahedral distortion.

Several examples of distorted octahedra have been reported in the literature, and the causes of such distortion are different in nature. The most common cause is the existence of an electronic instability associated with the presence of a d^0 cation. In these cases, the distortion can be attributed to the second-order Jahn−Teller (SOJT) effects. These effects occur when the empty d-orbitals of the metal are mixed with the filled p-orbitals of the oxide ligands. In condensed structures, this mixing results in a spontaneous distortion of the metal cation, which removes the near degeneracy of these two orbital sets, as occurs in $PbTiO_3$.[23] A different cause of the octahedral distortion is observed in $PbVO_3$,[24] which presents a highly distorted tetragonal perovskite structure ($c/a = 1.229$). In this case, the observation of such a distortion is driven by the tendency of the V^{4+} cations to form a strongly distorted octahedral coordination with one short vanadyl V−O distance, which results in a 5-fold coordination of the V atoms, stabilizing a square pyramid VO_5 instead the expected tridimensional framework of corner-sharing octahedra. The magnitude of the B-cations displacement in both examples is close to 0.5 Å, which is considerably larger than that exhibited by Ln atoms in the present case, between 0.150 and 0.175 Å (Figure 12). This fact plus the electronic configuration of Ln atoms reflects that the LnO_6 octahedral distortion in Pb_2LnSbO_6 is produced by the interaction between the metal and the oxygen anions that are linked to the lone-pair-bearing Pb atoms.

4.2. High-Temperature Crystal Structures and Phase Transitions. There is a different thermal evolution depending on the size of the lanthanide ion, as shown by the DSC profiles and the dielectric measurements (see Figures 2 and 3). The small rare-earth ions, Lu, Yb, and Tm, display three consecutive and reversible phase transitions with the same transition enthalpies ratios ($\Delta H_2/\Delta H_1 \approx 1.5$ and $\Delta H_2/\Delta H_3 \approx 10$), while the Er and Ho samples show the same two first transitions at the DSC curves with an enthalpy ratio of $\Delta H_2/\Delta H_1 \approx 5$. In this way, the behavior of the Pb_2LnSbO_6 family probably represents a break point for the Er compound, which additionally exhibits a tiny reversible peak in the DSC curves between the most energetic transitions.

The thermal evolution of the crystal structures for both types of perovskites, nicely represented by Pb_2YbSbO_6 and Pb_2HoSbO_6, differ in the absence of the P_γ polymorph for the second material. Therefore, the sequence followed by the Yb sample is $C2/c$ ($a^-b^-b^-$) → $P2_1/n$ ($a^-a^-b^+$) → $R\bar{3}$ ($a^-a^-a^-$) → $Fm\bar{3}m$ ($a^0a^0a^0$), whereas that observed for the Ho material is $C2/c$ ($a^-b^-b^-$) → $P2_1/n$ ($a^-a^-b^+$) → $Fm\bar{3}m$ ($a^0a^0a^0$). The thermal evolution of the unit-cell parameters for Ln = Ho, Er, and Yb in the entire range of temperatures is plotted in Figure 13. The P_β polymorph for either sample can be described as a commensurate $P2_1/n$ unit cell modulated by one or more wave-vectors. For the borderline compound with Ln = Er, the P_β polymorph region may even be of a more sophisticated structure, containing the regions of the temperature-independent (below T_3) and the temperature-dependent (above T_3) modulation. Probably, in the nature of this modulation lies the entire possible difference between the P_β structures for the compound with Ln = Ho and Yb. The indexation of the unsolved peaks is in progress.

This modulation could be related to Pb shifts, incommensurate with the octahedral network, as suggested by the facts that the modulation-related superstructure peaks are systematically stronger in the X-ray diffraction patterns compared to the neutron ones and that the isotropic displacement factors of lead atoms refined from the neutron powder data take considerably high values, of 3.5(2), 2.4(1), and 2.4(2) $Å^2$, for Ho, Er, and Yb, respectively. The P_β commensurate subcell is related to P_α through the c pseudocubic axis, taking into account the tilt system adopted for both polymorphic phases (P_α $a^-b^-b^-$ and P_β $a^-a^-b^+$). The DSC peak observed at T1 can be assigned to the change of the sign of θ_C, going from an antiphase to an in-phase arrangement.

The second phase transition observed for the Yb sample is related to the unification of the three tilt angles from the former $P2_1/n$ ($a^-a^-b^+$) arrangement to the rhombohedral $R\bar{3}$ ($a^-a^-a^-$) system. The tilting angles calculated were $\theta_A = \theta_B = \theta_C = -6.1°$. This merge of the tilting along the [111] pseudocubic direction induces the convergence of the previously defined O1, O2, and O3 oxygen atoms to one single oxygen atom in P_γ. This polymorph presents regular octahedra, with B−O bond lengths of 2.168 and 1.995 Å for YbO_6 and SbO_6, respectively. In addition, the lead polyhedra increase its coordination index from 8 to 9, and the observed geometry is consistent with the proposed criteria of Woodward[25] for tilt systems $a^-a^-a^-$, where the three closest anions form a perfect trigonal planar coordination in a plane perpendicular to the 3-fold axis, while the six other anions are arranged in a twisted trigonal prism about the A cation.

Finally, the last polymorph (P_δ) observed for the three compounds adopts a characteristic cubic double perovskite structure that can be viewed as an ordered stacking of LnO_6 and SbO_6 octahedra sharing corners without any tilting. Moreover, the space group symmetry ($Fm\bar{3}m$) imposes a total regularity of the octahedral sites (see Table 5). On the other hand, the lead atoms occupy the voids in between every eight octahedra, exhibiting 12-fold oxygen coordination. The observed Pb−O distances listed in Table 5 follow the same pattern and can be separated into three groups of longer [3.11(5), 3.12(1), 3.16(1) Å], medium [2.937(5), 2.95(4), 2.96(1) Å], and shorter distances [2.768(5), 2.79(4), 2.77(1) Å] for Ln = Yb, Er, and Ho, correspondingly. This pattern is consistent with previously reported cases of lead atoms displacement along the [111] cubic direction of the double perovskite. In these cases, the shifting

dx.doi.org/10.1021/ic200127a |*Inorg. Chem.* 2011, 50, 5545–5557

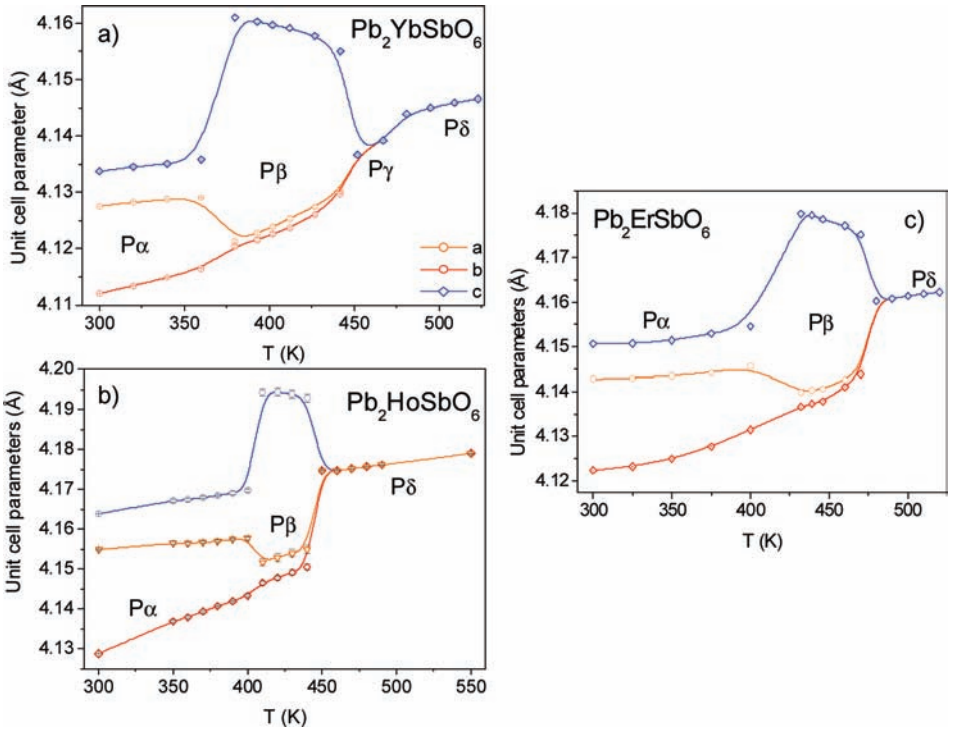

Figure 13. Thermal evolution for the whole investigated temperature range of the unit cell parameters taking into account the existent relationship with the aristotype for (a) Pb_2YbSbO_6, (b) Pb_2HoSbO_6, and (c) Pb_2ErSbO_6.

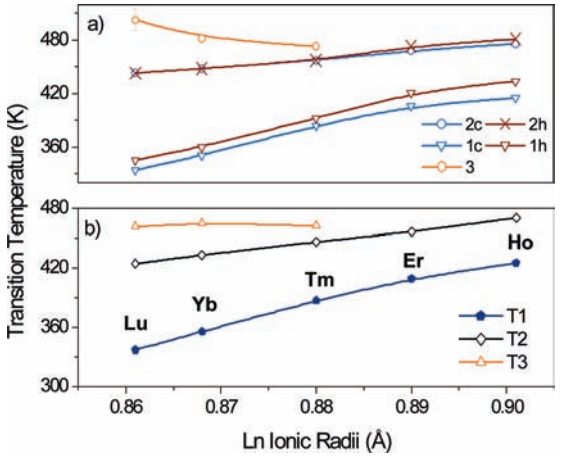

Figure 14. Dependences with the lanthanide ionic radii of the transition temperatures obtained from (a) dielectric permittivity measurements "c" is on cooling; "h" is on heating and (b) DSC curves.

with variable magnitudes occurs toward an octahedral face formed by three oxygen atoms. The calculated shifting magnitudes were 0.213(5), 0.20(4), and 0.24(1) Å for the Yb, Er, and Ho samples, respectively.

The relatively weak heat transfer corresponding to the different transitions obtained from the DSC curves (see Table 1) suggests that all the transitions are of displacive nature and are related to the overcoming of potential barriers between the two polymorphs involved in a specific phase transition. Furthermore, clear trends along the series are found for the phase transitions. These are displayed in Figure 14, where a steady decrease of the transition temperatures with the decrease in the lanthanide ionic size is shown. These trends are observed from both DSC curves and dielectric permittivity measurements. In addition, Figure S.9 (Supporting Information) shows the dependence of the enthalpy variation, ΔH_1 and ΔH_2, with the lanthanide size. From the smaller rare earths the enthalpy variation increases linearly with the increment of the lanthanide size from Lu to Tm; however, an opposite trend is shown for Er and Ho. This fact clearly evidences the effect of the modulation in the structure, which is different between both subgroups of compounds. On the other hand, from the values of the ΔH_2 data it is obvious that a greater tilting collapse ($a^-a^-b^+ \rightarrow a^0a^0a^0$) occurs at the last phase transition for the Ho and Er samples as compared to that at the ($a^-a^-a^- \rightarrow a^0a^0a^0$) transition for perovskites with the small lanthanide Ln = Tm, Yb, and Lu ions, which is reflected in the slope of the ΔH_2 dependence on the Ln ionic radii. Additionally, the samples that show no $R\bar{3}$ to $Fm\bar{3}m$ phase transition present an entropy variation associated with the last phase transition that is considerably greater than that related to the last entropy change of the samples with three phase transitions (see ΔS_2 data in Table 1). This fact is probably related to the greater structural difference that exists between a monoclinic $a^-a^-b^+$ structure and a cubic $a^0a^0a^0$ arrangement, compared to the observed difference between the rhombohedral $a^-a^-a^-$ and the cubic phase. Additionally, the diverse ΔS values associated with the last phase transition of the samples are in agreement with the thermal variation of the unit cell volume (see Supporting Information Figure S.10), where discontinuous changes are observed for the Er and Ho samples, while a steady increase is observed for the Yb sample.

The dielectric nature of the phase transitions can be analyzed from the dielectric measurements results. The Curie constants obtained for Tm, Yb, and Lu samples were 2.1×10^5, 1.5×10^5, and 1.9×10^5 K, respectively. These values are in the typical

dx.doi.org/10.1021/ic200127a |*Inorg. Chem.* 2011, 50, 5545–5557

range of displacive ferroelectric transitions and very close of that of $BaTiO_3$.[26] However, the negative value of the Weiss temperature strongly suggests that we are in the presence of an antiferroelectric transition coinciding with the last structural transition to a $Fm\bar{3}m$ cubic perovskite.[27] Moreover, strong evidence of the antiferroelectric nature of the rt polymorphs is that the displacements of lead ion are antiferroelectrically arranged, as shown in Figure S.11 (Supporting Information). The measured loops for Yb indirectly support the antiferroelectric nature of the less-symmetrical phases, since the threshold fields for antiferroelectric switching are often significantly higher than the coercive fields for ferroelectric reversal.[28] Note also the absence of nonlinearity in the effective permittivity (the average slope of the loop) in the 1−5 kV mm^{-1} range. Nonlinearity at subcoercive fields is a property of ferroelectrics, and a Rayleigh-type behavior has been described as a consequence of the ferroelectric domain wall dynamics.[29] This gives further support to the antiferroelectric nature of the transition.

5. CONCLUSIONS

The structural and thermal evolution of the four new members of the Pb_2LnSbO_6 family of perovskites has been followed from the NPD, DSC, and dielectric permittivity measurements. This family has resulted to be a very rich system from the crystallographic viewpoint, some peculiarities of which are still uncovered and will be the subject for further works. The rt crystal structure presents a severe monoclinic distortion, belonging to the $C2/c$ space group (isostructural to the multiferroic $BiMnO_3$) with unit cell parameters related to the aristotype ($a_0 \approx 4$ Å) as $a \approx c \approx \sqrt{6}a_0$ and $b \approx \sqrt{2}a_0$. This structure is characterized by three antiphase octahedral tiltings ($a^-b^-b^-$) and two different kinds of cation shifting: the first one related to the lead atom and the second one to the lanthanide ion inside the LnO_6 octahedron. The Ln = Lu and Yb perovskites display three successive phase transitions following the same thermal behavior as the previously reported Pb_2TmSbO_6 material: $C2/c \rightarrow P2_1/n$ (i) $\rightarrow R\bar{3} \rightarrow Fm\bar{3}m$ [the $P2_1/n$ (i) being an incommensurately modulated structure, which can be sufficiently well described in its commensurate subcell with the $P2_1/n$ symmetry]. Whereas the double-cubic perovskite is paraelectric, the permittivity measurements for Ln = Ho, Er, and Tm allowed concluding that the $R\bar{3}$ structures exhibit an antiferroelectric nature. In contrast, the Er- and Ho-containing perovskites show a different pattern of behavior, manifested in the DSC curves, the derived thermodynamic data, and the crystal structure evolution. These materials do not show the rhombohedral P_γ polymorph and probably exhibit a different modulation wave vector in the P_β phase. The structural sequence followed by these two compounds is $C2/c \rightarrow P2_1/n \rightarrow Fm\bar{3}m$, while for the Er-containing material, the P_β phase shows an even more complex structure, containing ranges with temperature-independent and the temperature-dependent modulations. The work on revealing the exact nature of the modulated phases is in progress.

■ ASSOCIATED CONTENT

Supporting Information. Figures S1−S11. This material is available free of charge via the Internet at http://pubs.acs.org.

■ AUTHOR INFORMATION

Corresponding Author
*E-mail: ja.alonso@icmm.csic.es.

■ ACKNOWLEDGMENT

S.A.L. is thankful for a CONICET fellowship. J.C.P. thanks CONICET (Project PIP N◦ 2008-01360), SECyT-UNSL (Project 7707), and ANPCYT (Project PICT 25459). J.C.P. is member of CONICET. J.A.A. acknowledges the financial support of the Spanish Ministry of Education to the project MAT2010-16404. The work is partially based on the results of experiments carried out at the Swiss spallation neutron source SINQ, Paul Scherrer Institut, Villigen, Switzerland.

■ REFERENCES

(1) Pearson, R. G. *J. Am. Chem. Soc.* **1969**, *91*, 4947.
(2) Pearson, R. G. *J. Mol. Structure (THEOCHEM)* **1983**, *103*, 25.
(3) Wheeler, R. A.; Whangbo, M.-H.; Hughbanks, T.; Hoffmann, R.; Burdett, J. K.; Albright, T. A. *J. Am. Chem. Soc.* **1986**, *108*, 2222.
(4) Iwanaga, D.; Inaguma, Y.; Itoh, M. *J. Solid State Chem.* **1999**, *147*, 291.
(5) Oka, K.; Azuma, M.; Hirai, S.; Belik, A. A.; Kojitani, H.; Takano, M.; Shimakawa, Y. *Inorg. Chem.* **2009**, *48*, 2285.
(6) Azuma, M.; Takata, K.; Saito, T.; Ishiwata, S.; Shimakawa, Y.; Takano, M. *J. Am. Chem. Soc.* **2005**, *127*, 8889.
(7) Baettig, P.; Spaldin, N. A. *Appl. Phys. Lett.* **2005**, *86*, 012505–8.
(8) Cascales, C.; Rasines, I.; García-Casado, P.; Vega, J. *Mater. Res. Bull.* **1985**, *20*, 1359.
(9) Unpublished results.
(10) Larrégola, S. A.; Alonso, J. A.; Pedregosa, J. C.; Martínez-Lope, M. J.; Algueró, M.; De La Peña-Shea, V.; Porcher, F.; Illas, F. *Dalton Trans.* **2009**, *28*, 5453.
(11) Larrégola, S. A.; Alonso, J. A.; Algueró, M.; Jiménez, R.; Suard, E.; Porcher, F.; Pedregosa, J. C. *Dalton Trans.* **2010**, *39*, 5159.
(12) Larrégola, S. A.; Alonso, J. A.; Sheptyakov, D.; Algueró, M.; Muñoz, A.; Pomjakushin, V.; Pedregosa, J. C. *J. Am. Chem. Soc.* **2010**, *39*, 5159.
(13) Woodward, P. M. *Acta Crystallogr. B* **1997**, *53*, 32.
(14) Rodríguez-Carvajal, J. *Physica B* **1993**, *55*, 192.
(15) Lufaso, M. W.; Woodward, P. M. *Acta Crystallogr B* **2001**, *57*, 725.
(16) Work in progress.
(17) Belik, A. A.; Iikubo, S.; Yokosawa, T.; Kodama, K.; Igawa, N.; Shamoto, S.; Azuma, M.; Takano, M.; Kimoto, K.; Matsui, Y.; Takayama-Muromachi, E. *J. Am. Chem. Soc.* **2007**, *129*, 971.
(18) Belik, A. A.; Iikubo, S.; Kodama, K.; Igawa, N.; Shamoto, S.; Maie, M.; Nagai, T.; Matsui, Y.; Yu, S.; Stefanovich; Lazoryak, B. I.; Takayama-Muromachi, E. *J. Am. Chem. Soc.* **2006**, *128*, 706.
(19) Walsh, A.; Watson, G. W. *J. Solid State Chem.* **2005**, *178*, 1422.
(20) Cheng, J.-G.; Zhou, J.-S.; Goodenough, J. B. *Phys. Rev. B* **2009**, *80*, 174426.
(21) Kimber, S. A. J.; Rodgers, J. A.; Wu, H.; Murray, C. A.; Argyriou, D. N.; Fitch, A. N.; Khomskii, D. I.; Attfield, J. P. *Phys. Rev. Lett.* **2009**, *102*, 046409.
(22) Halasyamani, P. *Chem. Mater.* **2004**, *16*, 3586.
(23) Bergman, J. G.; Crane, G. R.; Turner, E. H. *J. Solid State Chem.* **1977**, *21*, 127.
(24) Shpanchenko, R. V.; Chernaya, V. V.; Tsirlin, A. A.; Chizhov, P. S.; Sklovsky, D. E.; Antipov, E. V.; Khlybov, E. P.; Pomjakushin, V.; Balagurov, A. M.; Medvedeva, J. E.; Kaul, E. E.; Geibel, C. *Chem. Mater.* **2004**, *16*, 3267.
(25) Woodward, P. M. *Acta Crystallogr. B* **1997**, *53*, 44.
(26) *Principles and Applications of Ferroelectric and Related Materials*; Lines, M.E., Glass, A.M., Eds.; Clarendon Press: Oxford, 1977.
(27) Chandra, A.; Ranjan, R.; Singh, D. P.; Khare, N.; Pandey, D. *J. Phys.: Condens. Matter* **2006**, *18*, 2977.
(28) Park, Y.; Cho, K. *J. Am. Ceram. Soc.* **2000**, *83*, 135.
(29) Hall, D. A. *J. Mater. Sci.* **2001**, *36*, 4575.